Photoacoustics 28 (2022) 100417

Contents lists available at ScienceDirect

Photoacoustics

journal homepage: www.elsevier.com/locate/pacs

# High-speed wide-field photoacoustic microscopy using a cylindrically focused transparent high-frequency ultrasound transducer

Maomao Chen [a,1], Laiming Jiang [b,1,2], Clare Cook [a,1], Yushun Zeng [b], Tri Vu [a], Ruimin Chen [b], Gengxi Lu [b], Wei Yang [c], Ulrike Hoffmann [c], Qifa Zhou [b,*], Junjie Yao [a,*]

[a] Department of Biomedical Engineering, Duke University, Durham, NC 27708, USA
[b] Department of Biomedical Engineering, University of Southern California, Los Angeles, CA 90089, USA
[c] Multidisciplinary Brain Protection Program, Department of Anaesthesiology, Duke University School of Medicine, Durham, NC 27708, USA

ARTICLE INFO

*Keywords:*
High-speed imaging
Wide-field imaging
Optical-resolution photoacoustic microscopy
Cylindrically-focused ultrasound transducer
Transparent ultrasound transducer
Brain imaging

ABSTRACT

Combining focused optical excitation and high-frequency ultrasound detection, optical-resolution photoacoustic microscopy (OR-PAM) can provide micrometer-level spatial resolution with millimeter-level penetration depth and has been employed in a variety of biomedical applications. However, it remains a challenge for OR-PAM to achieve a high imaging speed and a large field of view at the same time. In this work, we report a new approach to implement high-speed wide-field OR-PAM, using a cylindrically-focused transparent ultrasound transducer (CFT-UT). The CFT-UT is made of transparent lithium niobate coated with indium-tin-oxide as electrodes. A transparent cylindrical lens is attached to the transducer surface to provide an acoustic focal line with a length of 9 mm. The excitation light can pass directly through the CFT-UT from the above and thus enables a reflection imaging mode. High-speed imaging is achieved by fast optical scanning of the focused excitation light along the CFT-UT focal line. With the confocal alignment of the optical excitation and acoustic detection, a relatively high detection sensitivity is maintained over the entire scanning range. The CFT-UT-based OR-PAM system has achieved a cross-sectional frame rate of 500 Hz over the scanning range of 9 mm. We have characterized the system's performance on phantoms and demonstrated its application on small animal models in vivo. We expect the new CFT-UT-based OR-PAM will find matched biomedical applications that need high imaging speed over a large field of view.

## 1. Introduction

Taking advantage of focused optical excitation and high-frequency ultrasound detection, optical-resolution photoacoustic microscopy (OR-PAM) can achieve an optically-defined lateral resolution of a few micrometers at depths of ~1 mm in biological tissues [1–3]. OR-PAM has been applied in many biomedical studies including cancer diagnosis, functional brain mapping, drug metabolism analysis, and circulating single cell detection [4–9]. Traditionally, OR-PAM systems use a point-by-point mechanical scanning scheme, in which the imaged sample or the imaging system is scanned to form a volumetric image. Although this method provides a large field of view (FOV), the mechanical scanning leads to a low imaging speed that cannot capture dynamic biological processes, such as the hemodynamic response to physiological challenges and pharmaceutical treatment. Therefore, there has been great interest in developing high-speed wide-field OR-PAM technologies.

Many efforts have been made by us and other groups to improve the imaging speed of OR-PAM using high-speed hybrid scanning methods. These hybrid scanning techniques usually acquire cross-sectional images by rapidly steering the excitation light along the fast axis and translating the sample or imaging probe along the slow axis. The excitation light and the resultant photoacoustic (PA) signal are confocally aligned and simultaneously steered along the fast axis using a galvanometer scanner [10–17], MEMS (microelectromechanical system) scanner [18–28], or polygon scanner [29,30]. Previous studies have demonstrated a B-scan frame rate of 1 kHz with a 10-mm scanning range [30,31], while maintaining high detection sensitivity. However, to achieve

* Corresponding authors.
*E-mail addresses:* qifazhou@usc.edu (Q. Zhou), junjie.yao@duke.edu (J. Yao).
[1] These authors contributed equally
[2] Current address: The College of Materials Science and Engineering, Sichuan University, Chengdu 610064, China.

https://doi.org/10.1016/j.pacs.2022.100417
Received 8 July 2022; Received in revised form 13 October 2022; Accepted 16 October 2022
Available online 17 October 2022

**Table 1**
Performances of PAM systems using TUTs.

| $F_C$ (MHz) | BW (MHz) | Light transmittance | Acoustic focusing | $R_{lat}$ (μm) | Scanning method | B-scan frame rate | Ref. |
|---|---|---|---|---|---|---|---|
| 14.5 | 10.2 | ~80% at 690–970 nm | Not focused | ~900 | Mechanical[a] | | [43] |
| 36.9 | 12.5 | > 80% at 450–1064 nm | Not focused | < 40 | Mechanical[a] | | [42] |
| 13 | 9.2 | ~90% at 532 nm | Not focused | 6.92 | Optical | 12.5 Hz over 3 mm | [44] |
| 24 | 26 | > 60% at 450–1100 nm | Spherically focused | 4.2 | Mechanical[a] | | [46] |
| 11.2 | 2.6 | ~66% at 700–900 nm | Spherically focused | 312 | Mechanical[a] | | [47] |
| 31.5 | 8 | > 70% at 500–750 nm | Spherically focused | 2.4 | Mechanical[a] | | [45] |
| 34 | 8.8 | ~50% at 532 nm | Cylindrically focused | 10 | Hybrid | 500 Hz over 9 mm | This work |

Fc, central frequency of the transparent ultrasound transducer; BW, bandwidth of the ultrasound transducer; $R_{lat}$, lateral resolution of the PAM system.
[a] The B-scan frame rate of mechanical scanning is determined by the laser pulse repetition rate (PRR) and the scanning speed of the motorized stage. Assuming a traditional PAM setup with a PRR of 1 kHz and a scanning speed of 10 mm/s, the typical B-scan frame rate of mechanical scanning is ~1 Hz over 10 mm.

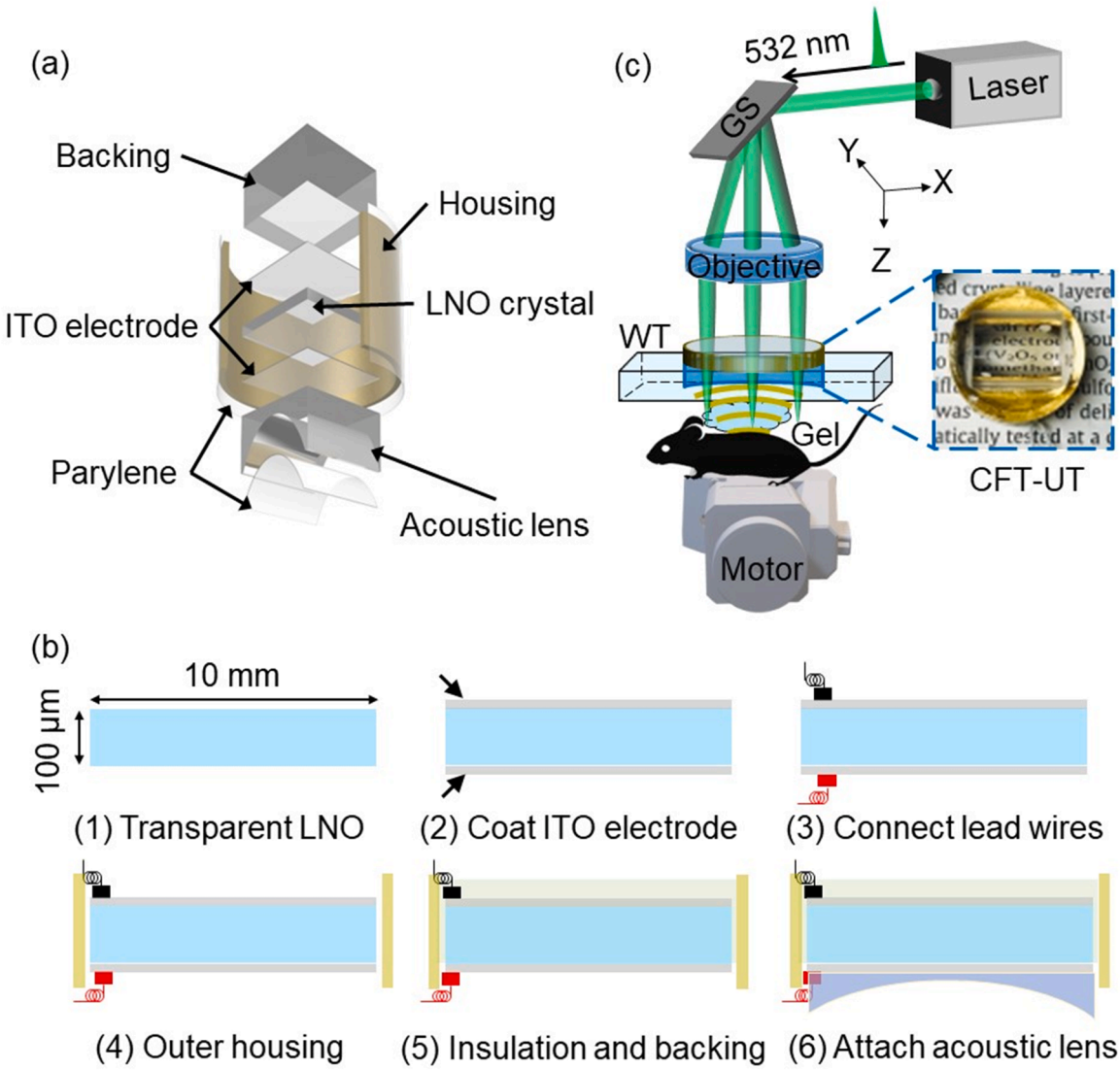


**Fig. 1.** Schematics of the CFT-UT PAM system. (a) Structure of the cylindrically-focused transparent ultrasound transducer (CFT-UT). LNO, lithium niobate. (b) The key fabrication steps of CFT-UT. (c) System schematic of CFT-UT PAM. GS, galvo scanner; Gel, ultrasound gel; WT, water tank. The inset photo shows the fabricated CFT-UT.

simultaneous steering of the optical and acoustic beams, the high-speed scanners need to be immersed in the acoustic coupling medium such as water. When the scanner is working at a high speed (e.g., vibrating the MEMS scanner or rotating the polygon scanner), the scanning stability and repeatability are often affected by the large damping force of water, which leads to deteriorated image quality and shortened scanner lifetime. Moreover, because the ultrasound transducer is typically non-transparent for light, an acoustic-optical combiner made of optical prisms and an acoustic lens is often needed to confocally align the excitation light beam and the resultant acoustic beam, which reduces the effective working distance, limits the numerical aperture of the optical objective, and often degrades the acoustic detection sensitivity.

Compared with the hybrid scanning mechanism that steers both the light and acoustic beams, pure optical scanning is usually simpler and more stable. In this method, the ultrasound transducer (flat or focused) is stationed in water, and the excitation light is steered over the detection zone of the ultrasound transducer [32–41]. Since acoustic beam steering is not needed, the optical scanner can operate in air, which is usually much faster and mechanically more stable than the hybrid scanning in water. One drawback of the optical scanning methods reported so far is that the ultrasound transducers, which are typically non-transparent, have small detection zone (for focused transducers) [32,33,35] or low detection sensitivity (for flat transducers) [36–41], and again usually need an optical/acoustic beam combiner.

Recently, transparent ultrasound transducers (TUT) have received increasing interest in OR-PAM as an alternative way to achieve optical/acoustic co-alignment without employing the beam combiner. Chen et. al reported a flat transparent ultrasound transducer with an optical transmission of ~90% in the visible-to-near-infrared spectrum [42]. Because this transducer is not focused, the detection sensitivity is relatively low [42–44]. Spherically focused transparent transducers demonstrate much better detection sensitivity [45,46], which, however, requires point-by-point mechanical scanning. Recently, a cranial window made of a transparent ultrasound transducer was developed to image the awake mouse brain [44]. It achieves a 12.5 Hz B-scan frame rate and a 0.03 Hz volumetric frame rate, but the imaging FOV is limited by the size of the cranial window to $3 \times 3$ mm$^2$. Table 1 summarizes recent works on PAM using TUTs.

Attempting to address the above issues, in this work, we report a high-speed wide-field OR-PAM system using a cylindrically focused transparent ultrasound transducer (CFT-UT), or CFT-UT PAM for short. The high imaging speed is enabled by fast optical scanning of the excitation light beam along the focal line of the CFT-UT. A B-scan rate of 500 Hz is achieved over a scanning range of 9 mm, which is majorly limited by the optical scanning speed of the galvo scanner. The fast optical scanning in the air provides excellent imaging stability, and the relatively high imaging sensitivity is achieved by the confocal alignment of the optical focal spot along the acoustic focal line. We have characterized the system's key performance on phantoms and demonstrated its dynamic imaging performance in vivo on small animals. We expect that CFT-UT PAM may provide an alternative solution for improving the imaging speed of OR-PAM with a large FOV.

## 2. Methods

### 2.1. Fabrication of the cylindrically-focused transparent ultrasound transducer

The CFT-UT schematic is shown in Fig. 1(a). A piece of transparent lithium niobate (LNO) (Boston Piezo-optics, MA, USA), with a length and thickness of 10 mm and 100 μm, respectively, was used as the core piezo-electric material. A thin layer of indium tin oxide (ITO) with a thickness of 100 nm was coated on both sides of the LNO using a dielectric sputter system (PVD750, Kurt Lesker, PA, USA). After the coaxial cable was connected to the upper and lower ITO electrodes with conductive silver paste (E-solder 3022), the LNO was packaged in a customized ring-shaped copper housing and fixed with a transparent backing layer made of epoxy with a thickness of 1 cm (Epotek 301). A transparent plano-concave cylindrical lens (LK1836L1, Thorlabs, Newton, NJ, USA) with a curvature of 5.0 mm was then attached to the bottom of the transparent LNO using transparent UV glue. The estimated one-dimensional focal length of the acoustic focusing is ~6.5 mm. Finally, a 10 μm thick parylene film (Parylene C, Specialty Coating Systems, Indianapolis, IN, USA) layer was vapor-deposited onto the external surface of the whole transducer package for protection and acoustic impedance matching. The key steps of the fabrication process of CFT-UT are summarized in Fig. 1(b).

### 2.2. CFT-UT PAM system

Fig. 1(c) shows the schematics of the CFT-UT PAM system. An Nd:YAG fiber laser (VPFL-G-20, V-Gen, Tel Aviv, Israel) provides the excitation light at 532 nm with a pulse width of 3 ns and a repetition rate of 800 kHz. The light beam is filtered by a pinhole (P25CB, Thorlabs, Newton, NJ, USA) with an aperture diameter of 25 μm, and then expanded to ~12 mm in diameter. The expanded beam is steered by a galvo scanner (GVS 002, Thorlabs, Newton, NJ, USA) to the back aperture of an objective lens with a focal length of 50 mm (AC254–050-A, Thorlabs, Newton, NJ, USA). The back focal point of the objective lens is coincident with the pivot point of the galvo mirror plate. The objective lens focuses the light beam through the CFT-UT on the surface of the target. To maximize the detection sensitivity, the optical focus and the acoustic focal line are confocally aligned along the scanning trajectory. To achieve volumetric imaging, the focused light beam is steered by the galvo scanner along the acoustic focal line of the transparent transducer (x-axis), and the slow axis (y-axis) is scanned using a motorized scanning stage (L-509, PI, Aubum, MA, USA). The galvo scanner is driven by a sinusoidal signal at 250 Hz. The scanning speed and scanning range can be flexibly adjusted by controlling the driving signal frequency and amplitude. The PA signals detected by the CFT-UT are amplified by two amplifiers (ZFL-500LN, Mini-Circuits, NY, USA) with a total gain of 50 dB and sampled with a sampling frequency of 250 MHz (ATS9350, Alazar Tech, Quebec, Canada).

### 2.3. CFT-UT PAM of mouse cortex vasculature

We performed in vivo imaging of the cortical vasculature of the mouse brain by the CFT-UT PAM system. To better image the vessels in the cortex, an optically- and acoustically- transparent transcranial brain window was used [31,48]. After surgically removing an approximately 8 mm by 8 mm area of the mouse skull, a 3D-printed cranial window with a frame size of 9 mm by 10 mm was installed on the skull. The window had an 8 mm by 7.5 mm clear aperture, which was sealed with thin PVC membrane [31]. The in vivo experiment was approved by the Institutional Animal Care and Use Committee of Duke University (protocol #: A126–21–06). The laser pulse energy applied on the surface of the transducer was 1 μJ, and the pulse repetition rate was 250 kHz. The fast-axis scanning step size was 8 μm and the slow-axis scanning step size was 5 μm. The galvo scanner was driven by a sinusoidal signal at 250 Hz, thus the B-scan frame rate was 500 Hz.

### 2.4. CFT-UT PAM of epinephrine-induced vasoconstriction in mouse ear

To demonstrate the high-speed wide-field imaging capabilities of the CFT-UT PAM system, we studied epinephrine-induced vasoconstriction in a mouse ear. Epinephrine is a widely used vasoconstrictor and blood pressure support medicine for treating cardiac arrest, asthma attacks and allergic reactions in an emergency situation [49,50]. The imaging settings were the same as the mouse cortex imaging. The mouse ear was first imaged for 5 min prior to the epinephrine injection to establish a baseline measurement. Then, we injected 5 μg of epinephrine through the tail vein of the mouse and imaged the mouse ear vasculature

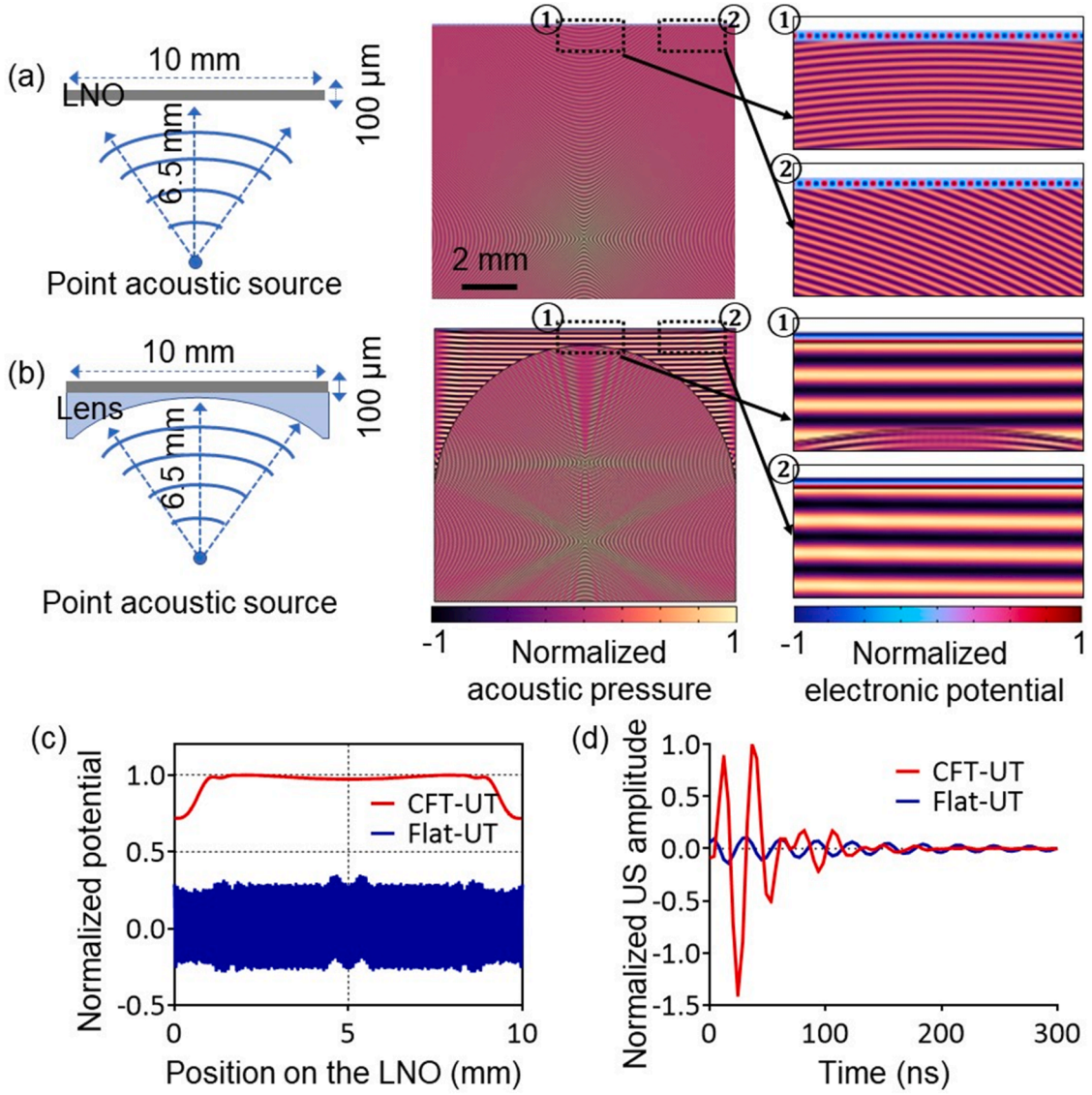


**Fig. 2.** Simulation of the detection sensitivities of the transparent transducer with and without the cylindrical lens. (a) The detection sensitivity of a flat transducer without the lens. (b) The detection sensitivity of a cylindrically focused ultrasound transducer with the lens. (c) Normalized acoustic potential extracted from (a) and (b). (d) The time-resolved ultrasound signal profile.

continuously for another 30 min. Each image frame took 5 s to cover an FOV of 6 × 9 $mm^2$.

## 3. Results

### *3.1. Simulation of the ultrasound detection by CFT-UT in photoacoustic imaging*

The detection sensitivity of CFT-UT is determined by both the piezoelectric material and the detection geometry. A finite element analysis (FEA) was performed using COMSOL (COMSOL Multiphysics 5.3a) to study the detection sensitivity of photoacoustic signals using the CFT-UT, as shown in Fig. 2. In the simulations, we compared the detection sensitivity of the CFT-UT without the cylindrical lens (Fig. 2 (a)) and with the lens (Fig. 2(b)). A point spherical wave was used to mimic the laser-induced photoacoustic pressure wave originated 6.5 mm from the transducer surface. Water was used as the coupling medium between the source and the transducer. When the ultrasonic waves reached the transducer surface, a piezoelectric potential was induced in the LNO plate due to the piezoelectric effect. In the simulations, we considered several physical fields including the pressure acoustics (frequency-domain), electrostatics, and solid mechanics, as well as the coupled interfaces of the piezoelectric effect and acoustic-structure boundary. We also considered the impedance mismatch between the selected materials in the simulation. The acoustic impedance of the water, cylindrical lens, and LNO crystal were set to 1.5, 17, and 34 Mrayls, respectively. Integrating the piezoelectric potential over the entire LNO surface provided a measurement of the detection by the CFT-UT.

The simulation results show that the ultrasound detection sensitivity was largely determined by the CFT-UT structure. Without the cylindrical lens, the detected acoustic waves on the flat LNO surface were out of phase, and the integration over the LNO surface resulted in relatively low signal amplitude and long signal duration. By contrast, with the cylindrical lens in front of the LNO plate, more acoustic waves reached to the LNO surface in phase. The clustered acoustic waves exhibited higher sound pressure levels on the LNO surface, inducing higher piezoelectric potentials. As shown in Fig. 2(b), the integrated piezoelectric potential with the cylindrical lens was higher than that without the lens. The normalized acoustic potential extracted from Fig. 2(a) and

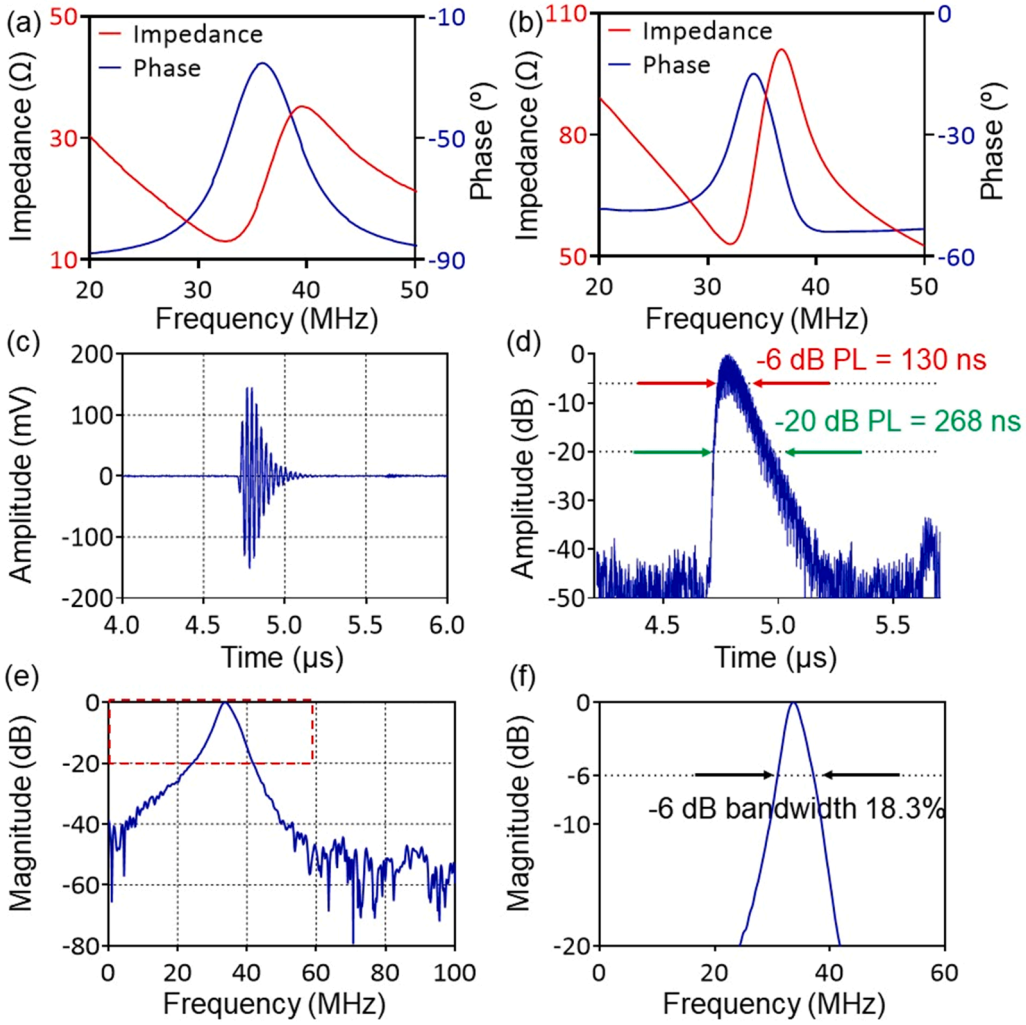


**Fig. 3.** Characterization of the CFT-UT prototype. (a, b) Simulated and measured impedance and phase spectra of the CFT-UT. (c) Pulse-echo signal on a quartz plate. (d) Pulse length measurement of the detected ultrasound echo signal. PL, pulse length. (e) Frequency response of pulse-echo signal. (f) Frequency bandwidth measurement of the CFT-UT in the pulse-echo mode.

2(b) was plotted in Fig. 2(c), showing a ~10 times higher detection sensitivity with the cylindrical lens. The improved detection sensitivity of the CFT-UT can also be observed from the time-resolved ultrasound signal profile as shown in Fig. 2(d). The received signal produced by the LNO with the cylindrical lens has a shorter oscillation period and a ~10 times higher ultrasound amplitude, which will result in a wider detection bandwidth and thus a higher axial resolution. As a result, the cylindrical lens can help improve the receiving sensitivity of the CFT-UT. Moreover, we studied the impedance mismatch between different materials. The estimated acoustic energy transmission ratio was 20% without the cylindrical lens, and 30% with the lens. Adding the lens between water and LNO plate actually improved the acoustic energy transmission, because the lens itself effectively served as an acoustic matching layer.

### 3.2. Characterization of the prototype CFT-UT

The CFT-UT based on transparent LNO piezoelectric crystal was designed with a theoretical center frequency at 34 MHz using PiezoCAD (Fig. 3(a)). The measured resonant frequency ($f_r$) and anti-resonant frequency ($f_a$) of the CFT-UT is ~32 MHz and ~37 MHz, respectively (Fig. 3(b)). The effective electromechanical coupling factor ($k_{eff}$) of the CFT-UT can be estimated as

$$k_{eff} = \sqrt{1 - \frac{f_r^2}{f_a^2}} \quad (1)$$

Thus, the value of our CFT-UT is ~0.5, which indicates a relatively high conversion efficiency between electrical and mechanical energy.

To measure the acoustic response of the fabricated CFT-UT, an ultrasound pulse was generated by the CFT-UT using an ultrasound pulse-receiver (DPR500-H01, Pittsford, NY, USA), with 1 μJ energy per pulse, 200 Hz pulse repetition rate, and 50 Ω damping factor. The transmitted ultrasound pulse was reflected by an X-cut quartz plate and measured by the CFT-UT. The echo signals were digitized at a sampling rate of 1 GHz/s. As shown in Fig. 3(c) and (d), the peak-to-peak amplitude of the received signal was ~300 mV, and the pulse length at − 6 dB and − 20 dB were 130 ns and 268 ns, respectively. The received pulse-echo signals were used to compute the frequency spectrum, shown in Fig. 3(e) and (f). The central frequency was ~34 MHz and the − 6 dB bandwidth was 18.3% or 6.2 MHz for the pulse-echo mode. The receiving-only bandwidth, as in photoacoustic imaging, should be 25.8% or 8.8 MHz. The optical transparency of the CFT-UT was ~50% at 532 nm, and the detection sensitivity, as evaluated as the noise equivalent pressure (NEP), was estimated to be 226.2 Pa over the detection bandwidth from 29.6 MHz to 38.4 MHz [51].

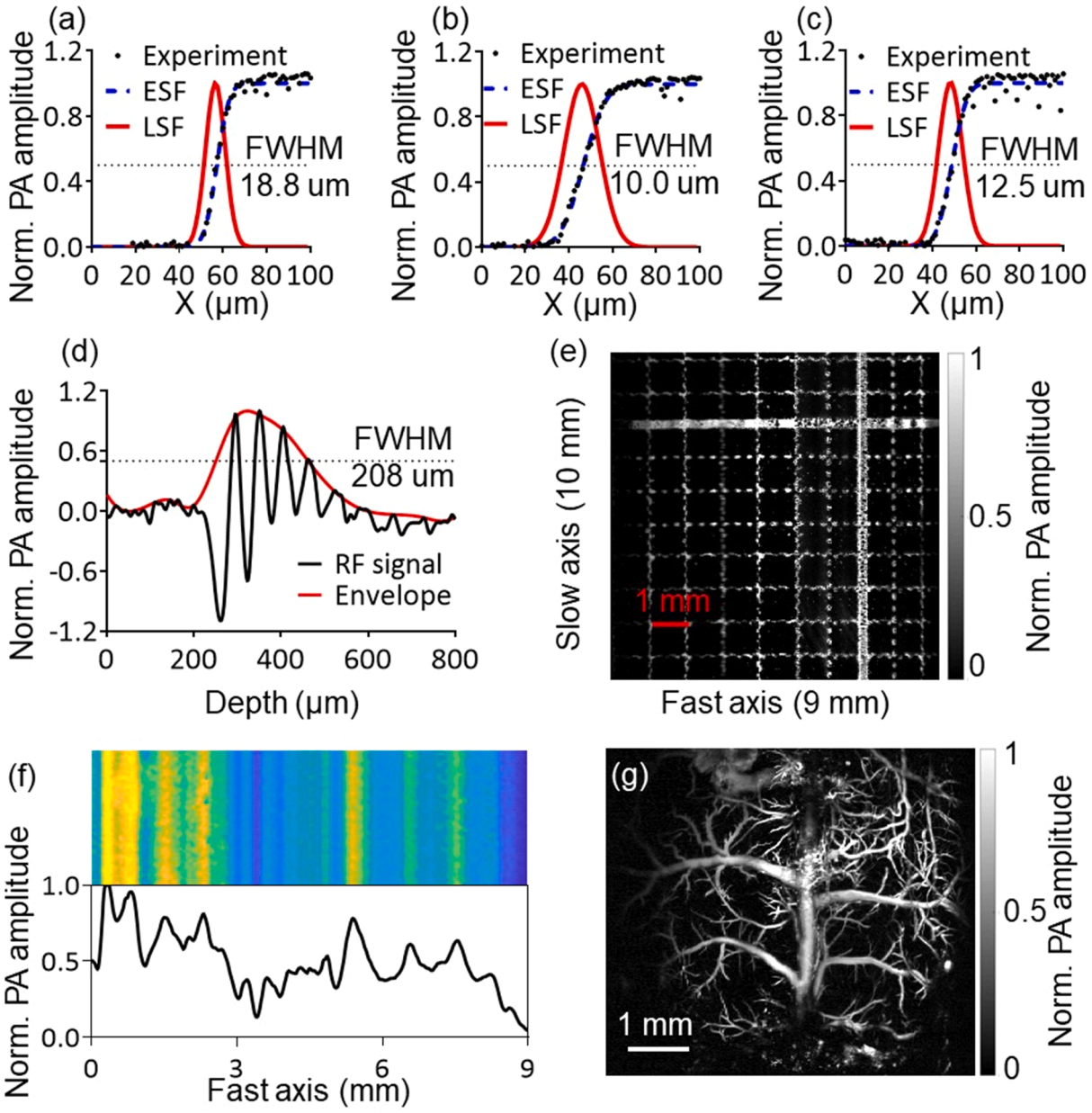


**Fig. 4.** Characterization of the CFT-UT-PAM system. (a)-(c) Lateral resolutions measured at different positions of the fast-scanning axis. (d) Measurement of the axial resolution from the envelope of the RF signal of a resolution target. (e) Scanning range along the fast-scanning axis. (f) Detection sensitivity distribution along the fast-scanning axis. (g) The PA image of the whole mouse cortex vasculature through a cranial window.

### *3.3. Characterization of the CFT-UT PAM system*

As the CFT-UT PAM system steers the excitation light along the CFT-UT's focal line (i.e., the fast axis), we quantified the lateral resolution, scanning range, and detection sensitivity along the fast-scanning path. The lateral resolution of the CFT-UT PAM system was measured by repeatedly scanning a sharp edge of the standard resolution target (R3L3S1P, Thorlabs) at different locations along the fast axis (Fig. 4(a)-(c)). We estimated the edge-spread function and line-spread function from the measurement data and quantified the lateral resolution as the FWHM of the line spread function. We performed the resolution measurement at three representative positions: the center and two ends of the fast scanning axis. The measured resolution varied from 18.8 μm at one end to 10 μm at the center and 12.5 μm at the other end. All three measurements were significantly larger than the theoretical resolution of 5 μm. There are two major reasons for the non-uniform and under-performed lateral resolution: (1) The backing layer of the CFT-UT has uneven thickness that leads to optical aberration; (2) The refractive index mismatch of the backing layer, LNO, and cylindrical lens induces additional optical aberration. As shown in Fig. 4(d), an envelope was extracted from the RF signal of a resolution target, and the axial resolution of CFT-UT PAM was measured as the FWHM of the envelope to be ~208 μm [52].

The scanning range was measured by imaging a printed target with a 1 mm by 1 mm grid size. We adjusted the driving voltage applied to the galvo scanner to maximize the scanning range along the fast axis to ~9 mm (Fig. 4(e)). The effective scanning and detection range were majorly limited by the size of the LNO plate. The scanning range along the slow axis was determined by the stepper motor stage, and thus was practically not limited.

The detection sensitivity uniformity over the FOV was measured by scanning a piece of uniform black tape (Fig. 4(f)). We extracted the

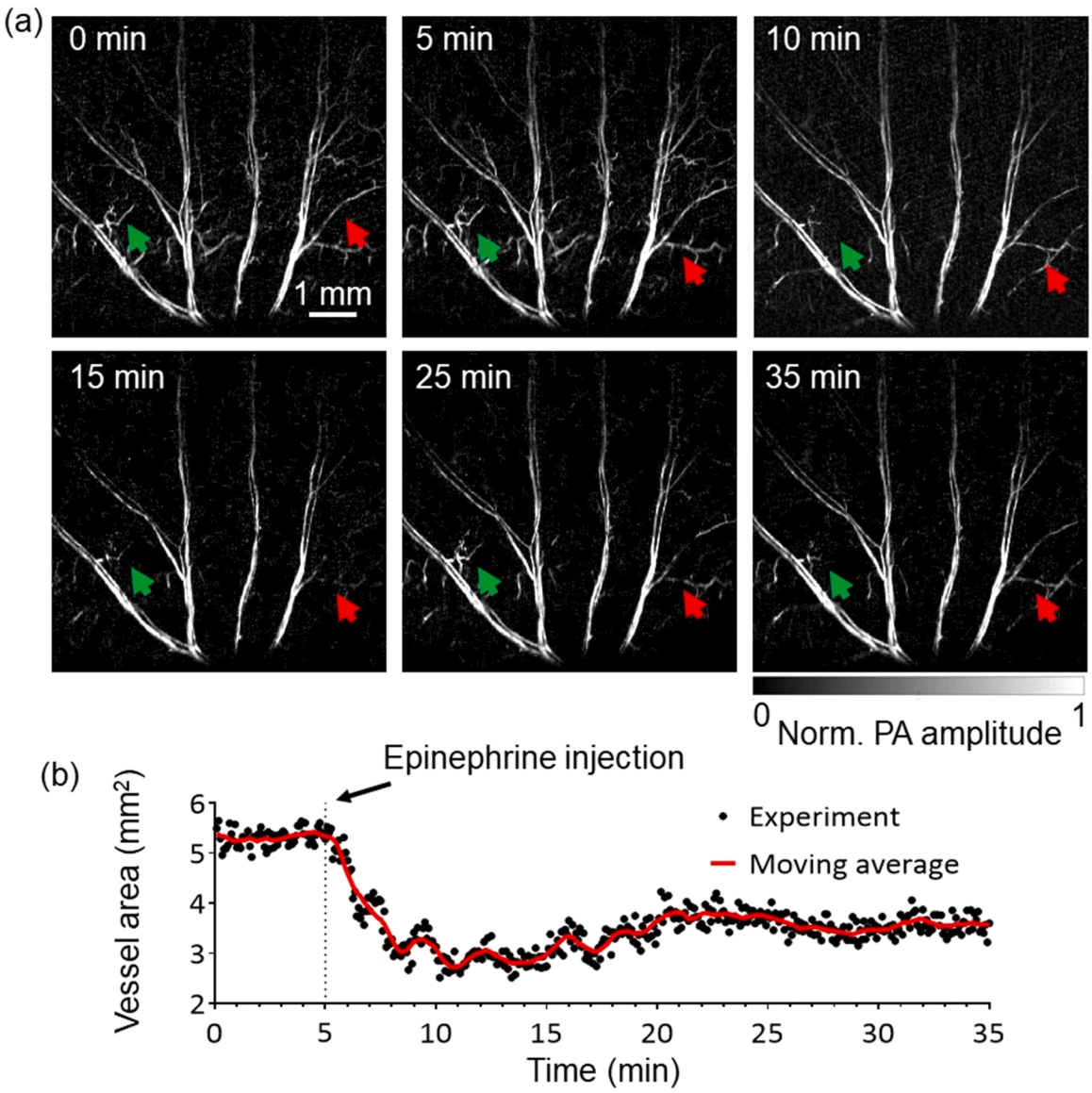


**Fig. 5.** CFT-UT PAM of the epinephrine-induced vasoconstriction in the mouse ear. (a) Representative PA images of the ear vasculature before and after epinephrine administration. The arrows highlight some microvessels that were constricted after the administration. (b) Quantitative analysis of the total vessel area. Each image took 5 s. The moving average (red line) was performed over 15 consecutive time points.

detected signals along the scanning range and calculated the relative standard deviation (rSD) of the detection sensitivity to be 60.88%. The relatively strong fluctuations in the detection sensitivity are mainly caused by the inconsistent optical focusing through the CFT-UT that leads to different optical spot size and thus different optical fluence. To partially address this issue, we covered the top surface of the backing layer of the CFT-UT with a thin layer of silicone oil, which slightly decreased the unevenness of the backing layer surface. Doing so, we reduced the rSD of the detection sensitivity to 38.70%.

After the characterization of the CFT-UT-PAM system, we demonstrated its in vivo imaging capability by mapping the whole cortical vasculature of the mouse brain with a cranial window. The in vivo image of the mouse cortical vasculature is shown in Fig. 4(g), which took only 5 s to scan an FOV of 6 × 6 $mm^2$. The major blood vessels were imaged with sufficient spatial resolutions. The non-uniform detection sensitivity of the system was not clearly observed from the in vivo image. Nevertheless, compared with traditional PAM systems with better spatial resolution and detection sensitivity [31,53], CFT-UT-PAM was not able to image as many microvessels that often have weaker PA signals.

### 3.4. CFT-UT PAM of epinephrine-induced vasoconstriction in mouse ear

Several representative snapshot PA images of the continuous monitoring are shown in Fig. 5(a). The total area of the major ear vasculature started at 5.5 $mm^2$ at the baseline (Fig. 5(b)). As expected, vasoconstriction was observed right after the administration of epinephrine. The total area of the main vasculature dropped by ~50% to 2.8 $mm^2$ at 10 min. Particularly, the major vessels became noticeably thinner due to vasoconstriction, while some microvessels disappeared entirely due to lack of blood perfusion. The vasculature then slowly returned to a total area of 3.9 $mm^2$ at 35 min as the drug effect of epinephrine slowly wore off. The dynamic change of the vasculature is shown in the Supplementary Video 1. The results were consistent with our previous results [30].

Supplementary material related to this article can be found online at doi:10.1016/j.pacs.2022.100417.

## 4. Conclusion and discussion

In this work, we have reported a new high-speed wide-field OR-PAM system using a cylindrically-focused transparent ultrasound transducer, or CFT-UT PAM. We investigated the optical and acoustic properties of the CFT-UT. The performance of the CFT-UT PAM system was characterized on phantoms, and its in vivo imaging capability was demonstrated by monitoring the hemodynamic changes on small animal models. In CFT-UT PAM, the excitation light beam was steered by a galvo scanner along the central focal line of the transparent transducer and achieved a large scanning range of 9 mm and a B-scan rate of 500 Hz. Although the CFT-UT PAM system has a similar B-scan rate as previously reported hybrid scanning systems [24,30], the pure optical scanning has achieved better imaging stability and repeatability, thus no post-imaging co-registration is required [31]. Because the optical-acoustic beam combiner is no longer needed, CFT-UT PAM has a simpler configuration than the traditional PAM systems. Moreover, with the confocal alignment of the optical focus and acoustic focal line, CFT-UT PAM has achieved better detection sensitivity than the previous system using a flat transparent transducer [42].

Although promising, the performance of the CFT-UT PAM system needs to be improved in several aspects. Firstly, the current prototype CFT-UT has non-uniform optical transparency and detection sensitivity along the acoustic focal line. This is largely due to the unevenness of the backing layer and can be improved by optimizing the fabrication process (e.g., laser cutting), reducing the backing thickness, or changing the backing materials (e.g., quartz). Secondly, the backing material is crucial to improve the transducer bandwidth. Conventional backing materials usually have high acoustic impedance and high sound attenuation, such as conductive silver paste and epoxy-tungsten powder blends, but low optical transparency. For transparent ultrasound transducers, a good backing material should have high acoustic impedance, high sound attenuation, as well as high optical transparency. There are two possible solutions to improve the bandwidth of our CFT-UT. (1). The bandwidth can be improved by using epoxy-hollow glass microsphere composite as the backing material. Although this composite has a lower acoustic impedance than conventional backing materials [54], it is optically transparent and has higher acoustic attenuation. (2). The bandwidth can be improved by bonding a right-angled prism directly to the back of the piezoelectric plate. The prism has high optical transparency, and the ultrasound waves can be directed away by the hypotenuse edge. Thirdly, the detection sensitivity of the CFT-UT is low compared with the spherically focused ultrasound transducer, thus a relatively high laser pulse energy was used in the in vivo experiments. This can be improved by increasing the size of the piezoelectric material, decreasing the focal length of the cylindrical lens, and improving the acoustic matching layers. Meanwhile, increasing the transducer size can also increase the maximum scanning range. Alternatively, structured illumination along the acoustic focal line may be adapted to improve the detection sensitivity [55]. Fourthly, the B-scan rate of CFT-UT PAM is determined by the scanning speed of the galvo scanner over a large scanning range, which can be improved by using faster optical scanners such as the polygon scanner [29,30]. Lastly, the light transmittance of the CFT-UT was only ~50% at 532 nm, which is relatively low compared with previously reported TUTs [42–47,56]. It can be improved by optimizing the sputtering process of the ITO electrodes on both sides of the LNO plate. Finally, high-speed functional PA imaging of blood oxygenation can be achieved by using dual-wavelength excitation based on the stimulated raman shifter [24,29,57].

## Declaration of Competing Interest

The authors declare that they have no known competing financial interests or personal relationships that could have appeared to influence the work reported in this paper.

## Data availability

Data will be made available on request.

## Acknowledgments

The authors would like to thank Prof. Zhongping Chen's team for the technical support on the ITO coating. This work was supported in part by American Heart Association Collaborative Sciences Award (18CSA34080277); National Institutes of Health (R01 EB028143, R01 NS111039, RF1 NS115581, R21 EB027304, R21 EB027981, R01 EB031629); National Science Foundation CAREER Award (2144788); Chan Zuckerberg Initiative Grant on Deep Tissue Imaging 2020–226178 by Silicon Valley Community Foundation.

## References

[1] K. Maslov, et al., Optical-resolution photoacoustic microscopy for in vivo imaging of single capillaries, Opt. Lett. 33 (9) (2008) 929–931.
[2] S. Hu, K. Maslov, L.V. Wang, Second-generation optical-resolution photoacoustic microscopy with improved sensitivity and speed, Opt. Lett. 36 (7) (2011) 1134–1136.
[3] R. Ma, et al., Fast scanning coaxial optoacoustic microscopy, Biomed. Opt. Express 3 (7) (2012) 1724–1731.
[4] S. Gottschalk, et al., Rapid volumetric optoacoustic imaging of neural dynamics across the mouse brain, Nat. Biomed. Eng. (2019).
[5] D. Razansky, et al., Multispectral opto-acoustic tomography of deep-seated fluorescent proteins in vivo, Nat. Photonics 3 (7) (2009) 412–417.
[6] L.H.V. Wang, S. Hu, Photoacoustic tomography: in vivo imaging from organelles to organs, Science 335 (6075) (2012) 1458–1462.
[7] A.P. Jathoul, et al., Deep in vivo photoacoustic imaging of mammalian tissues using a tyrosinase-based genetic reporter, Nat. Photonics 9 (4) (2015) 239–246.
[8] L.H.V. Wang, J.J. Yao, A practical guide to photoacoustic tomography in the life sciences, Nat. Methods 13 (8) (2016) 627–638.
[9] P. Hai, et al., High-throughput, label-free, single-cell photoacoustic microscopy of intratumoral metabolic heterogeneity, Nat. Biomed. Eng. (2019).
[10] J.Y. Kim, et al., High-speed and high-SNR photoacoustic microscopy based on a galvanometer mirror in non-conducting liquid, Sci. Rep. 6 (1) (2016), 34803.
[11] B. Rao, et al., Hybrid-scanning optical-resolution photoacoustic microscopy for in vivo vasculature imaging, Opt. Lett. 35 (10) (2010) 1521–1523.
[12] P. Hajireza, et al., Non-interferometric photoacoustic remote sensing microscopy, Light.: Sci. Appl. 6 (6) (2017) (9p. e16278-e16278).
[13] J. Kim, et al., Super-resolution localization photoacoustic microscopy using intrinsic red blood cells as contrast absorbers, Light.: Sci. Appl. 8 (1) (2019) 103.
[14] T. Wang, et al., Multiparametric photoacoustic microscopy of the mouse brain with 300-kHz A-line rate, Neurophotonics 3 (4) (2016), 045006.
[15] Y. Liang, et al., Fast-scanning photoacoustic microscopy with a side-looking fiber optic ultrasound sensor, Biomed. Opt. Express 9 (11) (2018) 5809–5816.
[16] J. Lee, et al., Fully waterproof two-axis galvanometer scanner for enhanced wide-field optical-resolution photoacoustic microscopy, Opt. Lett. 45 (4) (2020) 865–868.
[17] F. Yang, et al., Wide-field monitoring and real-time local recording of microvascular networks on small animals with a dual-raster-scanned photoacoustic microscope, J. Biophotonics 13 (6) (2020), e202000022.
[18] J. Yao, et al., Wide-field fast-scanning photoacoustic microscopy based on a water-immersible MEMS scanning mirror, J. Biomed. Opt. 17 (8) (2012), 080505.
[19] L. Lin, et al., High-speed photoacoustic microscopy of mouse cortical microhemodynamics, J. Biophotonics 10 (6–7) (2017) 792–798.
[20] C. Zhang, et al., Multiscale high-speed photoacoustic microscopy based on free-space light transmission and a MEMS scanning mirror, Opt. Lett. 45 (15) (2020) 4312–4315.
[21] X. Zhang, et al., Wide-angle structured light with a scanning MEMS mirror in liquid, Opt. Express 24 (4) (2016) 3479–3487.
[22] H. Guo, et al., Photoacoustic endomicroscopy based on a MEMS scanning mirror, Opt. Lett. 42 (22) (2017) 4615–4618.
[23] C. Lee, J.Y. Kim, C. Kim, Recent progress on photoacoustic imaging enhanced with microelectromechanical systems (MEMS) technologies, Micromachines 9 (11) (2018) 584.
[24] M. Chen, et al., High-speed functional photoacoustic microscopy using a water-immersible two-axis torsion-bending scanner, Photoacoustics (2021), 100309.
[25] J.Y. Kim, et al., Fast optical-resolution photoacoustic microscopy using a 2-axis water-proofing MEMS scanner, Sci. Rep. 5 (1) (2015) 7932.
[26] J.Y. Kim, et al., A PDMS-based 2-axis waterproof scanner for photoacoustic microscopy, Sensors 15 (5) (2015) 9815–9826.
[27] M. Moothanchery, et al., High-speed simultaneous multiscale photoacoustic microscopy, J. Biomed. Opt. 24 (8) (2019), 086001.
[28] K. Park, et al., Handheld photoacoustic microscopy probe, Sci. Rep. 7 (1) (2017), 13359.
[29] J. Chen, et al., Wide-field polygon-scanning photoacoustic microscopy of oxygen saturation at 1-MHz A-line rate, Photoacoustics (2020), 100195.

[30] B.X. Lan, et al., High-speed widefield photoacoustic microscopy of small-animal hemodynamics, Biomed. Opt. Express 9 (10) (2018) 4689–4701.
[31] X. Zhu, et al., Real-time whole-brain imaging of hemodynamics and oxygenation at micro-vessel resolution with ultrafast wide-field photoacoustic microscopy, Light.: Sci. Appl. 11 (1) (2022) 138.
[32] P. Hajireza, W. Shi, R.J. Zemp, Label-free in vivo fiber-based optical-resolution photoacoustic microscopy, Opt. Lett. 36 (20) (2011) 4107–4109.
[33] B. Rao, et al., Real-time four-dimensional optical-resolution photoacoustic microscopy with Au nanoparticle-assisted subdiffraction-limit resolution, Opt. Lett. 36 (7) (2011) 1137–1139.
[34] W. Shi, et al., In vivo near-realtime volumetric optical-resolution photoacoustic microscopy using a high-repetition-rate nanosecond fiber-laser, Opt. Express 19 (18) (2011) 17143–17150.
[35] X. Yang, et al., Fast axial-scanning photoacoustic microscopy using tunable acoustic gradient lens, Opt. Express 25 (7) (2017) 7349–7357.
[36] S. Jiao, et al., Simultaneous multimodal imaging with integrated photoacoustic microscopy and optical coherence tomography, Opt. Lett. 34 (19) (2009) 2961–2963.
[37] Z. Xie, et al., Laser-scanning optical-resolution photoacoustic microscopy, Opt. Lett. 34 (12) (2009) 1771–1773.
[38] S. Jiao, et al., Photoacoustic ophthalmoscopy for in vivo retinal imaging, Opt. Express 18 (4) (2010) 3967–3972.
[39] L. Xi, et al., Photoacoustic imaging based on MEMS mirror scanning, Biomed. Opt. Express 1 (5) (2010) 1278–1283.
[40] S.-L. Chen, et al., Miniaturized all-optical photoacoustic microscopy based on microelectromechanical systems mirror scanning, Opt. Lett. 37 (20) (2012) 4263–4265.
[41] F. Zhong, et al., High-speed wide-field multi-parametric photoacoustic microscopy, Opt. Lett. 45 (10) (2020) 2756–2759.
[42] R. Chen, et al., Transparent high-frequency ultrasonic transducer for photoacoustic microscopy application, IEEE Trans. Ultrason., Ferroelectr., Freq. Control 67 (9) (2020) 1848–1853.
[43] A. Dangi, S. Agrawal, S.-R. Kothapalli, Lithium niobate-based transparent ultrasound transducers for photoacoustic imaging, Opt. Lett. 44 (21) (2019) 5326–5329.
[44] S. Mirg, et al., Awake mouse brain photoacoustic and optical imaging through a transparent ultrasound cranial window, Opt. Lett. 47 (5) (2022) 1121–1124.
[45] J. Park, et al., Quadruple ultrasound, photoacoustic, optical coherence, and fluorescence fusion imaging with a transparent ultrasound transducer, Proc. Natl. Acad. Sci. USA 118 (11) (2021), e1920879118.
[46] C. Fang, H. Hu, J. Zou, A focused optically transparent PVDF transducer for photoacoustic microscopy, IEEE Sens. J. (2019) (p. 1-1).
[47] S. Park, S. Kang, J.H. Chang, Optically transparent focused transducers for combined photoacoustic and ultrasound microscopy, J. Med. Biol. Eng. 40 (5) (2020) 707–718.
[48] T.H. Kim, et al., Long-term optical access to an estimated one million neurons in the live mouse cortex, Cell Rep. 17 (12) (2016) 3385–3394.
[49] S.F. Kemp, et al., Epinephrine: the drug of choice for anaphylaxis – a statement of the World Allergy Organization, World Allergy Organ. J. 1 (2) (2008) S18.
[50] M. Shoroghi, et al., Effect of different epinephrine concentrations on local bleeding and hemodynamics during dermatologic surgery, Acta Dermatovenerol. Croat. 16 (4) (2008), p. 0-0.
[51] J. Yao, L.V. Wang, Sensitivity of photoacoustic microscopy, Photoacoustics 2 (2) (2014) 87–101.
[52] J.J. Yao, L.H.V. Wang, Photoacoustic microscopy, Laser Photonics Rev. 7 (5) (2013) 758–778.
[53] J.J. Yao, et al., High-speed label-free functional photoacoustic microscopy of mouse brain in action, Nat. Methods 12 (5) (2015) 407 (-+).
[54] G. Gao, et al., Acoustic and dielectric properties of epoxy resin/hollow glass microsphere composite acoustic materials, J. Phys. Chem. Solids 135 (2019), 109105.
[55] J. Liang, et al., Spatially Fourier-encoded photoacoustic microscopy using a digital micromirror device, Opt. Lett. 39 (3) (2014) 430–433.
[56] Z. Li, A.K. Ilkhechi, R. Zemp, Transparent capacitive micromachined ultrasonic transducers (CMUTs) for photoacoustic applications, Opt. Express 27 (9) (2019) 13204–13218.
[57] Y. Liang, et al., 2 MHz multi-wavelength pulsed laser for functional photoacoustic microscopy, Opt. Lett. 42 (7) (2017) 1452–1455.

**Maomao Chen** Maomao Chen is a postdoctoral research fellow in the BME department at Duke University. He received his Ph. D. degree from the Medical School of Tsinghua University, Beijing, China in 2017. His current research interest focuses on the system development and biological application of photoacoustic imaging.

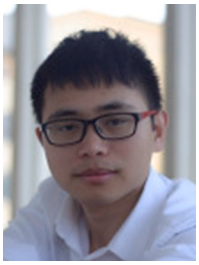

**Laiming Jiang** Dr. Laiming Jiang received his Ph.D. degree in Materials Physics and Chemistry from Sichuan University, in 2019. He worked as a postdoctoral scholar - research associate in the Keck School of Medicine at the University of Southern California, in 2020–2021. He is currently an assistant professor in the College of Materials Science and Engineering at Sichuan University. His research work focuses on the development of high-performance piezoelectric materials, piezoelectric ultrasound transducers, ultrasound bioimaging, ultrasound-induced energy harvesting, multiscale and multimaterials 3D printing, and bio-implantable devices.

**Clare Cook** I am originally from Eagle River, Alaska and completed my bachelor's degree in Electrical Engineering from Princeton University (2020). My undergraduate research focused on the miniaturization of imaging systems, and I hope to grow my knowledge of device design and imaging systems while pursuing my Ph.D. at Duke.

**Tri Vu** Tri Vu received his bachelor's degree in Biomedical Engineering from State University of New York at Buffalo. He is currently a Ph.D. candidate at Department of Biomedical Engineering in Duke University. His research interests are high-speed small-animal photoacoustic imaging systems and photoacoustic image enhancement using deep learning.

**Ruimin Chen** Ruimin Chen received the B.S. degree in biomedical engineering from the University of Electronics Science and Technology of China, Chengdu, China, in 2006, and the M.S. and Ph.D. degrees in biomedical engineering from the University of Southern California, Los Angeles, CA, USA, in 2008 and 2014, respectively. He was a Postdoctoral Research Associate and the Resource Manager with the NIH Ultrasonic Transducer Resource Center, Department of Biomedical Engineering, University of Southern California, where he was also a Research Specialist with the USC Roski Eye Institute. He was an Ultrasound Sensor Engineer with Masimo Corporation, Irvine, CA, USA. He is currently an Associate Researcher with the Research Center for Humanoid Sensing, Zhejiang Lab, Hangzhou, China. His research interests include the design, modeling, and fabrication of high-frequency ultrasonic transducers and arrays for biomedical and industrial imaging applications.

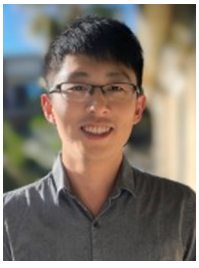

**Gengxi Lu** Gengxi Lu received the bachelor's degree in physics from Nanjing University, Nanjing, China, in 2017. He is currently pursuing the Ph.D. degree with the Department of Biomedical Engineering, University of Southern California, Los Angeles, CA, USA. His research interests include the ultrasound neuromodulation, ultrasound imaging and elastography, 3-D printing, and the development of ultrasound transducers.

**Wei Yang** Wei Yang is an associate professor in the Department of Anesthesiology at Duke University Medical Center. He received a B.S. degree from Wuhan University (China), a M.S. degree from Institute of Microbiology (Chinese Academy of Science), and a Ph.D. degree from University of Rostock (Germany). His current research interest is centered on ischemia/reperfusion injury after ischemic stroke and cardiac arrest.

**Ulrike Hoffmann,** M.D. Ph.D. Ulrike Hoffmann is an assistant professor of Anesthesiology in Duke Health and physician-scientist interested in the pathophysiology of stroke and acute brain injury. She has received M.D., Ph.D. and board certification in anesthesiology in Germany, completed her postdoctoral research in Harvard University and joined the clinical faculty in Duke University in 2015. Her basic science laboratory is now focused on cerebral blood flow during anesthesia and resuscitation in acute brain injury rodent models and translation into the human setting.

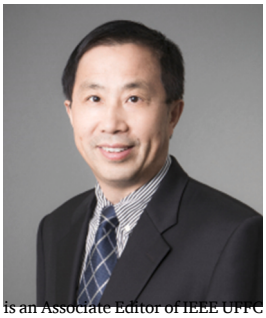

**Qifa Zhou** Prof. Zhou received his Ph.D. degree from the Department of Electronic Engineering at Xi'an Jiaotong University. He is currently a Research Professor at the NIH Resource on Medical Ultrasonic Transducer Technology and the Departments of Biomedical Engineering and Ophthalmology at USC. Before joining USC in 2002, he worked in the Materials Research Laboratory at Pennsylvania State University. Prof. Zhou is a Fellow of SPIE and AIMBE, a senior member of the IEEE Ultrasonics, Ferroelectrics, and Frequency Control (UFFC) Society, and a member of the Ferroelectric Committee, UFFC in IEEE. He is also a member of the technical program Committee of IUS in IEEE and Photoacoustic Committee in SPIE. He is an Associate Editor of IEEE UFFC and Chapter Chair in IEEE UFFC from 2015. He was the co-author of a paper that received the best student paper competition award in 2010 IEEE IUS and the best poster paper in photoacoustic plus ultrasound in 2015 SPIE Photonics West. He has published more than 170 journal papers in these areas.

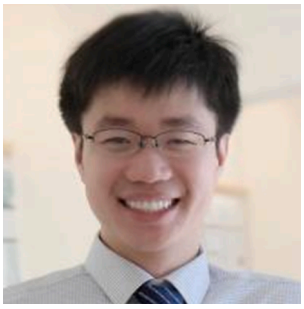

**Junjie Yao** Prof. Dr. Junjie Yao is currently Assistant Professor at the Department of Biomedical Engineering, Duke University. Dr. Yao received his B.S. (2006) and M.S. (2008) degrees in Biomedical Engineering from Tsinghua University (Beijing, China), and his Ph.D. degree in Biomedical Engineering at Washington University in St. Louis in 2013. More information about Dr. Yao's research at http://photoacoustics.pratt.duke.edu/